



First production of X-rays at the ThomX high-intensity Compton source

Marie Jacquet^{1,a} , Patrick Alexandre², Muath Alkadi¹, Manuel Alves¹, Manar Amer¹, Loic Amoudry¹⁴, Didier Auguste¹, Jean-Luc Babigeon¹, Philippe Balcou¹⁰, Michel Baltazar¹, Chamseddine Benabderrahmane¹⁵, Rachid Ben el Fekih², Alain Benoit¹, Philippe Berteaud², Marica Biagini⁵, Alexandre Blin¹, Sébastien Bobault², Marco Bonanzingamarco²⁰, Jean Bonenfant¹, Julien Bonis¹, Yazid Bouanani², Said Bouaziz¹¹, François Bouvet², Alberto Bravin^{7,8}, Christelle Bruni¹, Cyril Bruyere³, Harold Bzyl⁴, Lodovico Cassinari², Kevin Cassou¹, Jean-Noël Cayla¹, Thomas Chabaud¹, Iryna Chaikowska¹, Sophie Chance¹, Christophe Chappelle⁴, Vincent Chamat¹, Ronic Chiche¹, Alain Cobessi³, Eric Cormier¹⁷, Patrick Cornebise¹, Marie-Emmanuelle Couprie², Renaud Cuoq², Olivier Dalifard¹, Jérôme Degallaix¹⁹, Nicolas Delerue¹, William Del Net³, Antonio Diaz², Yannick Dietrich², Massamba Diop², Remy Dorkel¹, Denis Douillet¹, Ilya Drebot⁵, Jean-Phillipe Dugal¹, Kevin Dupraz¹, Eric Dupuy², Moussa El Ajjouri², Nouredine El Kamchi¹, Mohamed El Khaldi¹, Hélène Elleaume⁹, Ezgi Ergenlik¹, François Estève⁹, Pierre Favier¹, Marco Fernandez¹, Alexis Gamelin², Jean-François Garaut¹, Luca Garolfi¹, Philippe Gauron¹, Frédéric Gauthier¹, Pascal Girault¹⁸, Alexandre Gonnin¹, Denis Grasset¹, Eric Guerard¹, Hayg Guler¹, Jacques Haissinski¹, Jean-Louis Hazemann³, Dias Helder², Christian Herbeaux², Emmanuel Herry¹, Jean-Louis Hodeau³, Jean-Michel Horodyski⁴, Nicolas Hubert², Gregory Iaquaniello¹, Philippe Jacquet³, Philippe Jeantet³, Didier Jehanno¹, Eric Jules¹, Grigor Kapoujyan³, Viacheslav Kubytskyi¹, Marie Labat², François Labaye¹², Jerome Lacipière³, Mickaël Lacroix¹¹, Eric Lahéra³, Marc Langlet³, Titouan Lebarillec¹, Jean-François Ledu¹, Géraldine Le Duc¹⁶, Damien Le Guidec¹, Bruno Leluan¹, Pierre Lepercq¹, Alain Lestrade², Frédéric Letellier-cohen¹, Antoine Letrésor², Jérôme Lhermite¹⁰, Xing Liu¹³, Robert Lopes², Alexandre Loulergue², Marc Louvet², Christophe Mageur¹, Patrick Marchand², Rodolphe Marie¹, Jean-Claude Marrucho¹, Fabrice Marteau², Aurélien Martens¹, Gabriel Mercadier¹, Bruno Mercier¹, Christophe Michel¹⁹, Eric Mistretta¹, Hugues Monard¹, Alexandre Moutardier¹, Didier Muller², Amor Nadjji², Laurent Nadolski², Ryutaro Nagaoka², Olivier Neveu¹, Daniele Nutarelli¹, Maher Omeich¹, Dominique Pedeau², Yann Peinaud¹, Gilles Perroux³, Antoine Pérus¹, Sylvain Petit², Yannick Petrilli¹, Marc Pichet¹, Bernard Pieyre¹, Laurent Pinard¹⁹, Eric Plaigne¹, Jean Pierre Pollina², Christophe Prévost¹, Olivier Proux³, Fernand Ribeiro², Pierre Robert⁴, Manuel Ros², Thomas Roulet¹, Raphael Roux¹, Emmanuel Roy³, Philippe Rudnicki¹, Julien Salvia², Mourad Sebdaoui², Serge Sierra¹⁸, Viktor Soskov¹, Rajesh Sreedharan², Jean Susini², Monique Taurigna-Quéré¹, Stéphane Trochet¹, Cynthia Vallerand¹, Alessandro Variola⁵, José Veteran², Olivier Vitez¹, Philippe Walter⁶, François Wicak¹, Sébastien Wurth¹, Fabian Zomer¹

¹ IJCLab, CNRS/IN2P3, Université Paris-Saclay, Orsay, France

² SOLEIL Synchrotron, Saint-Aubin, France

³ Institut Néel, CNRS, Université Grenoble Alpes, Grenoble, France

⁴ IRSD, CNRS, Université Paris-Saclay, Orsay, France

⁵ INFN, Rome, Italy

⁶ LAMS, CNRS, Sorbonne Université, Paris, France

⁷ University of Milano-Bicocca, Milano, Italy

⁸ University of Calabria, Rende, Italy

⁹ STROBE, INSERM, Université Grenoble Alpes, Grenoble, France

¹⁰ CELIA, CNRS/CEA, Université de Bordeaux, Talence, France

¹¹ IRFU, CEA, Université Paris-Saclay, Gif-sur-Yvette, France

¹² LTF, Université de Neuchâtel, Neuchâtel, Switzerland

¹³ DEP, Tsinghua University, Beijing, China

¹⁴ RADIABEAM, Santa Monica, CA, USA

¹⁵ ESRF Synchrotron, Grenoble, France

¹⁶ NH TherAguix SAS, Villeurbanne, France

¹⁷ LP2N, CNRS, Université de Bordeaux, Bordeaux, France

¹⁸ THALES, Vélizy, France

¹⁹ LMA, CNRS, Université de Lyon, Villeurbanne, France

²⁰ IRSN, Fontenay-aux-Roses, France

Received: 25 January 2024 / Accepted: 16 April 2024

© The Author(s), under exclusive licence to Società Italiana di Fisica and Springer-Verlag GmbH Germany, part of Springer Nature 2024

^a e-mail: marie.jacquet@ijclab.in2p3.fr (corresponding author)

Abstract With the increase in laser power and finesse of optical cavities over the last decade, laboratory-size Compton sources are very promising. These sources produce X-rays through interactions between relativistic electrons and laser photons and, in term of brightness, fall between large synchrotron facilities and classical laboratory X-ray sources. The ThomX source is the French project in this field. This article first presents a state of the art of high-intensity Compton sources, then the ThomX source is briefly described, and the first results are detailed, in particular the production of the first X-rays, the acquisition of the first spectrum and the first image of the beam. Finally, the next objectives are discussed.

1 Introduction

In many fields of science, synchrotron radiation sources are currently the only machines available to carry out the most ambitious analyses and research requiring a high-brightness X-ray beam in the 10 – 100 keV energy range. But synchrotron facilities are not very practical. For example, in materials science, transporting a valuable work of art or a crystal cooled with liquid nitrogen presents high costs and dangers. Furthermore, access to them is limited, whereas the needs in many scientific fields are growing. In the medical field in particular, the lack of access to synchrotron facilities considerably limits the development of *in vivo* studies required before large-scale clinical application. Although progress in the construction of increasingly powerful laboratory sources is significant, the most efficient rotating anode tubes currently provide $\sim 10^9 - 10^{10}$ X-rays/s at limited and non-tunable X-ray energies. These sources are not suitable for specific studies requiring a higher level of performance, and, for a wide class of applications, the flux is too low and therefore requires prohibitively long exposure times.

Compact Compton sources (CCS) are modestly sized machines ($\sim 100 \text{ m}^2$) that can be integrated in a room-sized space. Their development would make it possible to fill the significant gap in terms of brightness between conventional laboratory sources and synchrotron facilities. The principle of a Compton source is based on the production of X-rays pulses by inverse Compton backscattering of intense laser light against electron bunches. Today, CCS aiming to deliver flux larger than $10^{11} - 10^{12}$ ph/s are in full development thanks to the improvement of high-power lasers over the last decades. Numerous experiments realized today only at the large synchrotron facilities in the fields of medicine (imaging and therapy), biology, cultural heritage (studies and preservation) or industry could be carried out within a laboratory, a museum or an hospital [1–4].

ThomX is the French project of such a source. It is a demonstrator aiming at producing, ultimately, 10^{13} ph/s with a brightness of $10^{11} \text{ ph}/(\text{s} \cdot \text{mm}^2 \cdot \text{mrad}^2)$ in 0.1% of bandwidth, in the energy range 45 – 90 keV. The project supported and managed by IJCLab (Laboratoire de physique des 2 infinis - Irène Joliot-Curie) is based on the Orsay campus at the Paris-Saclay university and is in its commissioning phase.

After a brief introduction to the basic principles of a Compton source, this article first highlights the key parameters required to produce a high-brightness beam and presents the state of the art in high-intensity CCS. Next, the ThomX source is described and the main results obtained since the startup of the commissioning phase are presented, in particular the production of the first X-ray beam and the few preliminary measurements that followed. Finally, the next steps of the commissioning phase and the perspectives are discussed.

2 State of the art of high-intensity CCS

2.1 Compton source principles

The inverse Compton scattering process is shown schematically in Fig. 1. A relativistic electron moving along the z-axis interacts with a laser photon in the x-z plane. In the collision, a part of the energy of the electron is transmitted to the photon. The kinematics of the process can be described as a collision of two particles, or using the synchrotron radiation analogy, as an electron traveling through the “micro-undulator” of the electromagnetic field of a photon. The energy E_X of the scattered photon in the laboratory frame can be expressed by a general formula taking into account the recoil of the electron (Compton regime) as [2]: $E_X = E_L(1 + \beta \cos \theta_c) / [1 - \beta \cos \theta_X + E_L(1 + \cos \theta_c \cos \theta_X + \sin \theta_c \sin \theta_X \cos \phi_X) / E_e]$, where β is the relativistic factor of the electron, E_e the electron energy, E_L the energy of the incoming photon, and θ_c , θ_X and ϕ_X the incident angle and the scattering polar and azimuthal angles with respect to the electron direction. When E_L is small compared to rest mass energy of the electron, the recoil of the electron can be neglected (Thomson regime); then the formula of the scattered photon energy becomes:

$$E_X = \frac{2\gamma^2 E_L (1 + \cos \theta_c)}{1 + \gamma^2 \theta_X^2}, \quad (1)$$

where $\gamma = E_e / m_e c^2$ is the electron Lorentz factor, m_e the electron mass, c the speed of light. To derive expression (1), it was also assumed that $\gamma \gg 1$. Many inverse Compton sources meet these two conditions ($E_L \ll m_e c^2$ and $\gamma \gg 1$), and it is the case for the ThomX source.

Equation (1) implies an univocal dependence between the energy E_X of a backscattered photon and its scattering angle θ_X : the X-rays show a distribution in the form of concentric cones where the energy decreases as one moves away from the center.

Fig. 1 Diagram of the inverse Compton scattering process between an electron of energy E_e and a photon of energy E_L having an angle of incidence θ_c with respect to the direction of the electron

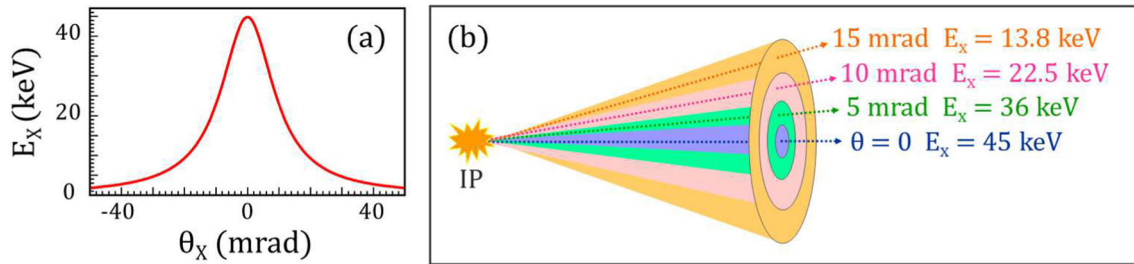
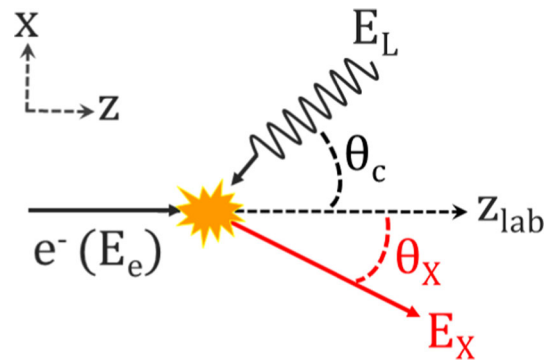


Fig. 2 Energy/angle relation of backscattered Compton photons. **a** Energy of Compton photons as a function of their scattering angle for head-on collisions of laser pulses of wavelength of $1.03 \mu\text{m}$ with electron bunches of 50 MeV . **b** Schematic illustration of the concentric cones of the Compton beam. IP is the interaction point

Those produced forward ($\theta_x = 0$) have the maximum energy $E_m = 2\gamma^2 E_L(1 + \cos \theta_c)$, known as "Compton edge". So, a simple diaphragm placed on the axis of the Compton cone allows a small energy band to be selected. Figure 2 shows the X-ray energy/angle distribution and illustrates the correlation.

For electrons traveling along the longitudinal z direction, the number of Compton photons produced per second in all energy bandwidth and all solid angles is noted F_{tot} and is written as follows [5]:

$$F_{\text{tot}} = \frac{\Sigma_{\text{th}} N_e N_L F_{\text{rep}}}{2\pi [(\sigma_e^2 + \sigma_L^2) + \tan^2(\theta_c/2)(\sigma_{ze}^2 + \sigma_{zL}^2)]^{1/2} [(\sigma_e^2 + \sigma_L^2)]^{1/2}}, \tag{2}$$

where Σ_{th} is the Thomson cross section, N_e and N_L , respectively, the numbers of electrons per bunch and the number of photons per laser pulse, F_{rep} the repetition frequency of the interactions and $\sigma_e, \sigma_L, \sigma_{ze}$ and σ_{zL} the transverse and longitudinal dimensions (r.m.s.) of the electron bunch and laser pulse at the interaction point. The transverse size σ_S of the source is written as follows [6, 7]:

$$\sigma_S = \frac{\sigma_L \sigma_e}{\sqrt{\sigma_L^2 + \sigma_e^2}}. \tag{3}$$

To derive expressions (2) and (3), vertical and horizontal transverse beam dimensions were assumed to be the same and Gaussian.

The source brightness is defined as:

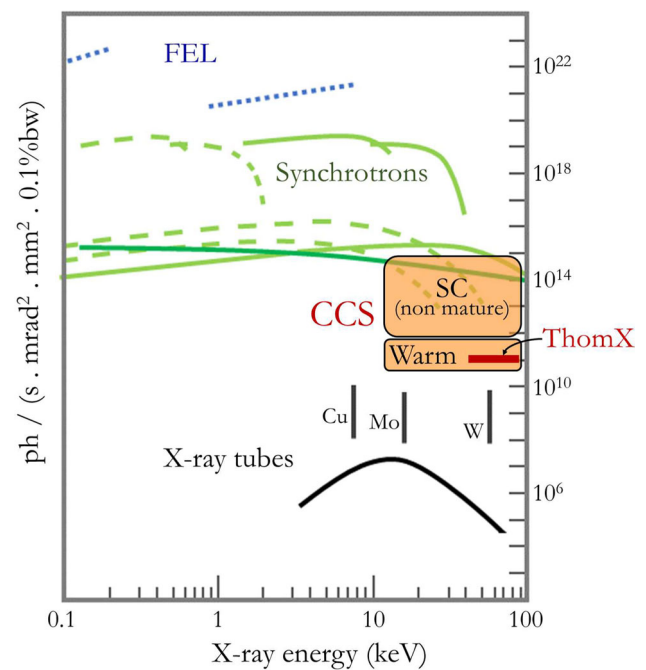
$$Br = \frac{F_{0.1\%}}{4\pi^2 \sigma_S^2 \sigma_S'^2}, \tag{4}$$

where $F_{0.1\%} = 1.5 \times 10^{-3} F_{\text{tot}}$ is the X-ray flux in a 0.1% bandwidth at the Compton edge, σ_S and σ_S' are the transverse size and divergence of the source respectively. The performances of current electron beams and laser systems are such that the main impact on the X-ray beam quality comes from the characteristics of the electron beam [2, 6–8], and the brightness can then be written as follows:

$$Br \sim \frac{F_{0.1\%}}{4\pi^2} \left(\frac{\gamma^2}{\epsilon_N} \right) \left(1 + \frac{\sigma_e^2}{\sigma_L^2} \right), \tag{5}$$

where ϵ_N is the normalized transverse emittance of the electron beam: $\epsilon_N = \gamma \sigma_e \sigma_e', \sigma_e'$ being the divergence of the beam. As shown by expression (5), the emittance of the electron beam is the crucial parameter for a source to deliver high brightness.

Fig. 3 Typical source brightnesses as a function of X-ray energy for synchrotron facilities, conventional laboratory sources and CCS projects targeting a flux greater than $\sim 10^{11} - 10^{12}$ ph/s (orange squares). "SC" stands for sources based on superconducting technology (including the electron gun); "Warm" stands for sources based on the conventional accelerator technology and using a storage ring. The nominal brightness of the ThomX project is indicated



2.2 Challenges of high-intensity Compton sources

Thanks to advances in lasers, optical cavities and accelerators, Compton sources could now produce more than 10^{12} X-rays/s provided that the average power of the interacting laser is of the order of a few hundred kW. On the electron side, a few mA of average current are required, or just a few tens of μA if the electron bunches have a transverse size of a few micrometers at the interaction point.

To achieve an electron current of a few mA, the repetition frequency must be of the order of several tens of MHz. Let us give a concrete example: 10^{13} ph/s can be obtained with a repetition frequency F_{rep} of 20 MHz, an electron bunch charge of 500 pC, laser pulses of 10 mJ and a transverse dimension of the two incident beams of 40 μm . Two machine designs based on Compton backscattering allow this high repetition rate to be achieved, depending on whether the laser photons collide with electrons from a small storage ring of around ten meters in circumference, or with those from a superconducting linear accelerator. In the case of a storage ring, F_{rep} is determined by the revolution frequency of the electrons in the ring. In this scheme based on well-known "warm" technology, typical maximum reachable fluxes and brightnesses are $10^{12} - 10^{13}$ ph/s and $10^{10} - 10^{11}$ ph/(s · mm^2 · mrad²) in 0.1% of bandwidth, respectively. In the linear accelerator-based scheme without a storage ring, the repetition frequency is determined by the injection frequency of the electron source which must necessarily be a superconducting device to deliver continuously the required electron current. The brightnesses can then reach $10^{14} - 10^{15}$ ph/(s · mm^2 · mrad²) in 0.1% of bandwidth thanks to the very low emittance values of the electron beam (of the order of 0.1 – 0.5 mm.mrad) that the superconducting gun is capable of producing. Although electron injector projects aimed at delivering an average current of a few mA are currently in development, superconducting technology in that field is not yet mature enough to achieve both the rate and number of electrons required [9, 10]. Superconducting linear accelerator-based machines offer by far the highest brightness but currently still face many technical challenges and, in addition, will require much greater radiation protection. However, for many X-ray applications (especially in the medical field), brightness is not the critical parameter; more important is the available flux in a given solid angle [11, 12].

In the panorama of hard X-ray sources (10 – 100 keV), the positioning of CCS projects based on warm and superconducting technologies aiming to produce more than $10^{11} - 10^{12}$ ph/s is shown in Fig. 3. Currently, the most powerful CCS in the world is the MuCLS source which was developed and manufactured by Lyncean Technologies Inc. and which deliver $\sim 10^{11}$ ph/s full bandwidth in the 15–35 keV range [13, 14]. Over the past fifteen years, several CCS projects have been launched with the aim of producing $> 10^{12}$ ph/s. Some of them have adopted the storage ring scheme [15–19], others the linac scheme with superconducting injection elements [20–26], while another uses a novel room-temperature X-band linac coupled to a cryogenic laser system for Compton collisions [27]. Among these projects, ThomX is well advanced and could reach the 10^{12} ph/s threshold in the near future.

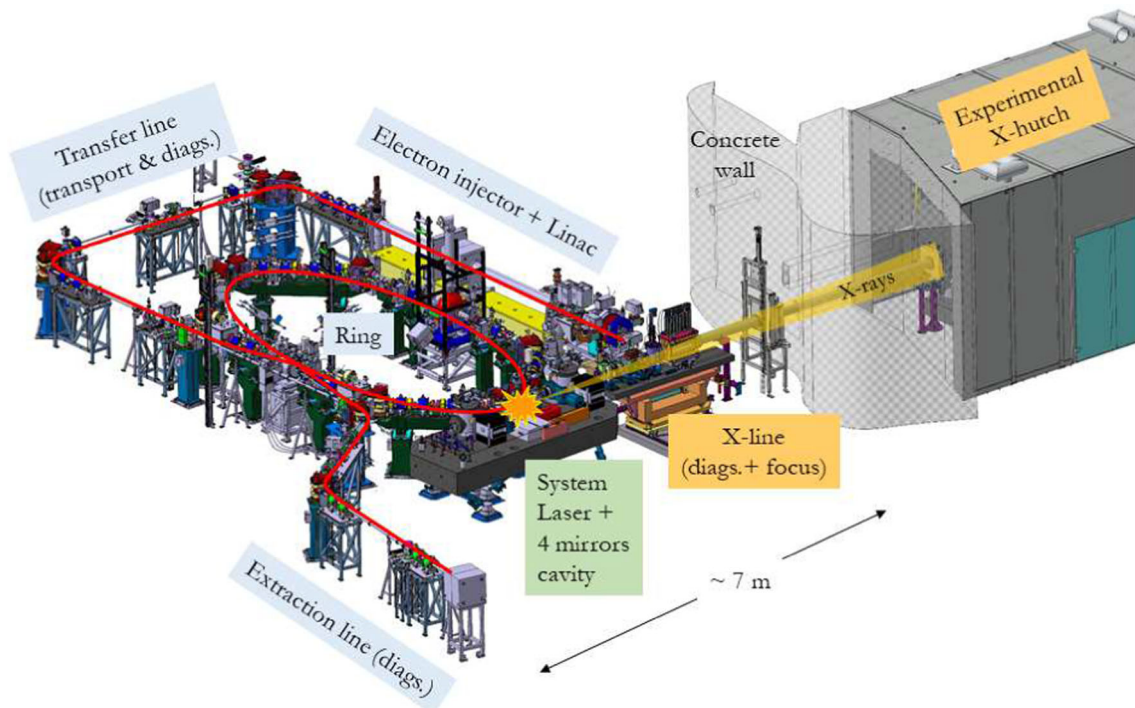


Fig. 4 The ThomX source layout

3 The ThomX project

3.1 Presentation of the machine

The layout of the ThomX source is presented in Fig. 4. Electron bunches of 1 nC charge with an energy of ~ 5 MeV are first emitted by an RF photocathode gun at a repetition frequency of 50 Hz by the impact of 257 nm laser pulses on a copper or magnesium cathode (injector). Each bunch propagates in a linear accelerator (linac) which increases its energy to 50 – 70 MeV. A transfer line adapts the bunch for its injection and storing in a small ring, 17.8 m in circumference. Only one bunch travels in the ring at a given time. After 20 ms, the bunch degraded by Compton collisions and collective effects is ejected toward a dump which absorbs it (extraction line) and is replaced by a new one¹. The nominal normalized emittance ϵ_N of the electron beam is 5 – 10 mm.mrad. At the interaction point, the electron bunch transverse size σ_e is ~ 70 μm . The laser system is placed on an optical table, itself resting on a hexapod controlled at the micrometric level and which allows the laser pulses to be positioned on the path of the electrons. The system consists of a 1030 nm laser oscillator emitting pulses, amplified by a fiber amplifier, then stacked in a four-mirrors Fabry–Perot cavity, these two amplification stages leading to a nominal power permanently stored in the optical cavity of the order of 700 kW. The nominal transverse size of the laser pulses at the interaction point is $\sigma_L \sim 40$ μm . At the interaction point, the two incident beams have a length of around 10 ps and cross every 60 ns with an angle of incidence θ_c equal to 2 degrees. A precise synchronization system was developed to coordinate all subsystems of the machine (injector, linac, ring, pulsed magnetic elements, laser, diagnostics devices).

For radiation protection purposes, the machine is located inside a shielding zone, the bunker, made up of thick concrete walls (a section of wall can be seen in Fig. 4).

With the nominal parameters mentioned above, the expected flux F_{tot} in full spectral bandwidth is of $\sim 10^{13}$ X-rays/s in the energy range 45 – 90 keV (on-axis), the transverse source size of ~ 35 μm and the brightness of 10^{11} ph/(s \cdot mm² \cdot mrad²) in 0.1% of bandwidth. The angular aperture available for the X-ray beam is constrained by the mechanics of the Fabry–Perot cavity which delimits a maximum opening half-angle of 7 mrad.

3.2 The X-ray beamline

The X-ray beamline aims on the one hand to monitor and shape the Compton beam and on the other to carry out experiments in order to demonstrate the potential and the limits of the ThomX demonstration prototype. The line is divided into two distinct parts. The first part, shown in Fig. 5, consists of a motorized optical table located inside the bunker on which simple and robust systems are positioned for a continuous monitoring of the beam and for its shaping (beam shutter, double slits to select desired beam sizes,

¹ The injection and extraction are performed by a septum and two fast kickers <https://theses.hal.science/tel-03850856>.

Fig. 5 First part of the X-line located in the bunker. 1: Beam shutter. 2: Slits. 3: Fluorescent screen detector. 4: Kapton diffusion detector. 5: Tungsten wire monitor. 6: Motorized table. 7: Focusing device (transfocator)

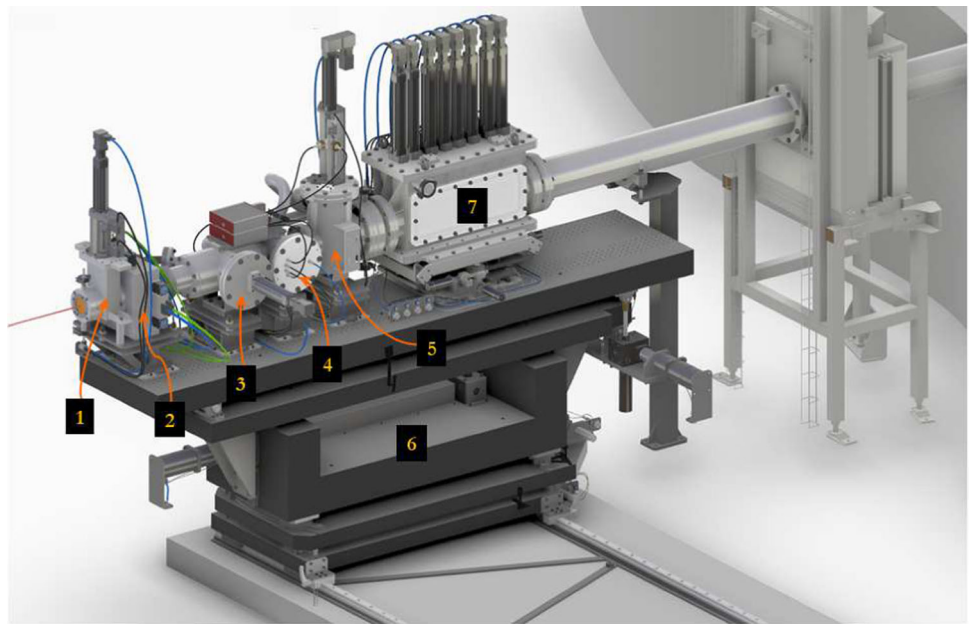
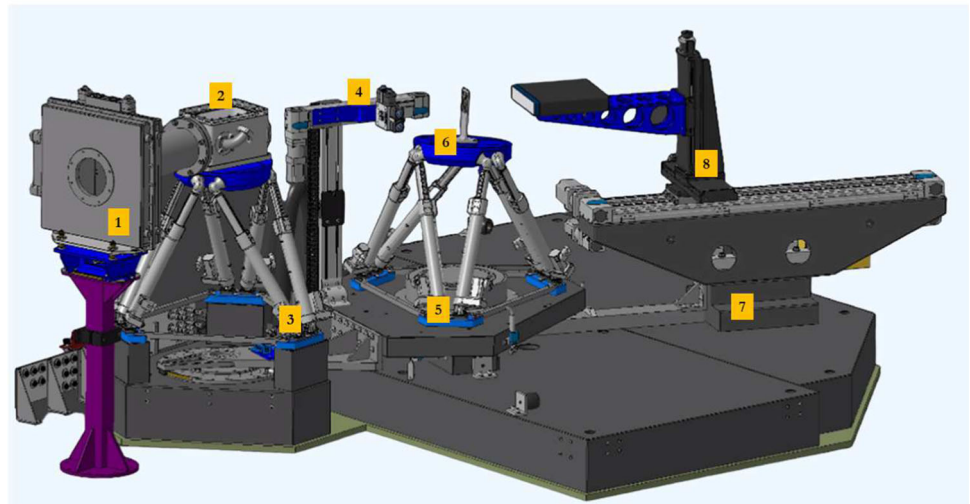


Fig. 6 Second part of the X-line located in the experimental hutch. 1: Slits ($150 \times 150 \text{ mm}^2$ of total aperture). 2: Monochromator. 3: Monochromator positioning hexapod. 4: Slits ($30 \times 30 \text{ mm}^2$ of total aperture, retractable). 5: Sample positioning hexapod. 6: Tomography rotating stage. 7: Goniometer. 8: Detector positioning system



fluorescent screen detector, Kapton diffusion detector, wire monitor). At the end of this table, an optical device (a transfocator [28]) is installed in order to be able to make parallel or focus the beam at the sample position (in ThomX, samples are positioned at approximately 10 m from the interaction point). The second part of the line is installed inside the experimental X-hutch area after the safety beam shutter and the concrete wall of the accelerator bunker. X-rays travel from the bunker to the experimental area through a 150 mm diameter vacuum beam pipe. This second part of the line consists of a modular device which should allow on the one hand to determine the performances and limits of the source for imaging in the medical and material science fields, and on the other hand to highlight its possibilities in the structural analysis of materials by experiments combining diffraction, diffusion and spectroscopy. The experimental setup, presented in Fig. 6, combines various elements (two sets of slits to clean the beam selected in the bunker by the first slits, a monochromator, two hexapods, a goniometer and translation and rotation motors) which will be used or not depending on the analysis technique implemented.

4 Results

Technical studies and simulations of the characteristics and parameters expected for safety and radiation protection, for the accelerator, the laser interaction system, the diagnostic equipment, the synchronization system and the X-ray beamline are detailed in [29, 30]. Following the phases of civil engineering for the infrastructures, construction and delivery of the equipment, and integration of the subsystems inside the building, the commissioning of the machine began at the end of 2021 when the French Nuclear Safety Agency

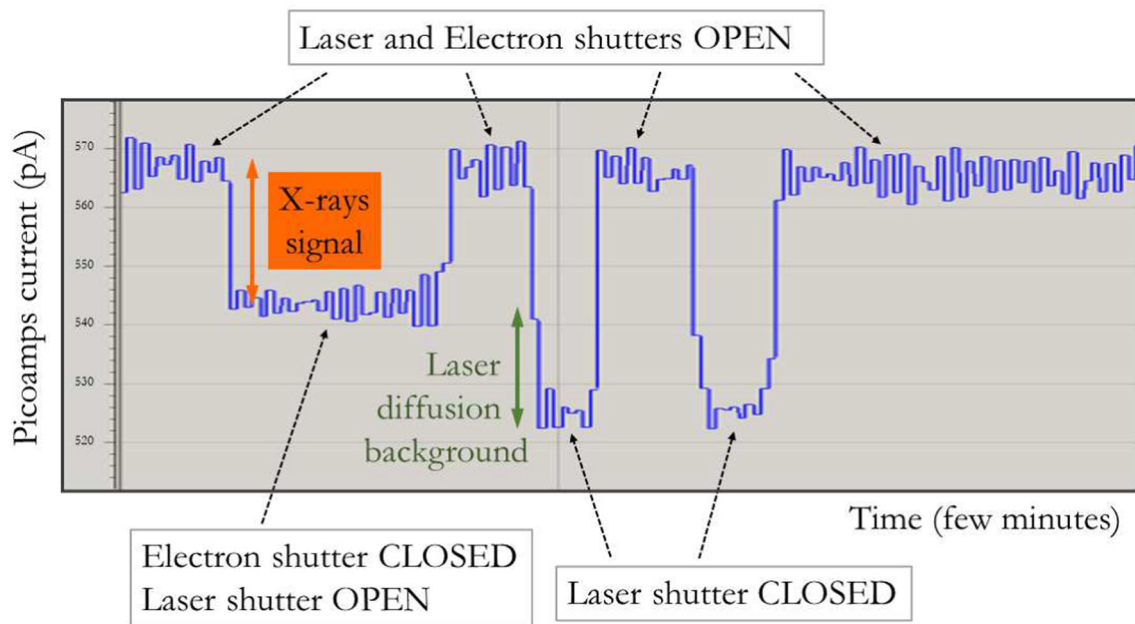


Fig. 7 First X-rays signal obtained at the ThomX source and cross-checks to ensure that signal is due to X-rays

(ASN) gave its authorization. Today, the charge and energy of the electron bunches authorized by the ASN are limited to 100 pC and 50 MeV, respectively, and the electron gun injection frequency to 10 Hz.

4.1 Accelerator and laser system commissioning

Electron bunches of 100 pC are currently produced by the photoinjector at a repetition frequency of 10 Hz, focused and fully transmitted to the end of the accelerating section with an energy of 50 MeV [31].² Each bunch is transported to the ring by the transfer line, injected and stored in the ring for 100 ms before being dumped in the extraction line [32]. The first diagnostic elements essential for properly aligning and storing the beam are operational enabling the charge and position of the bunches to be measured throughout the accelerator [33]. All these accelerator devices are coordinated in time by the synchronization system [34]. The interaction laser is locked in the high finesse Fabry–Perot cavity [35, 36] in the difficult and noisy environment of the accelerator, and the stored power is today ~ 30 kW and will be increased gradually to avoid the risk of mirror breakage.

4.2 First X-rays production

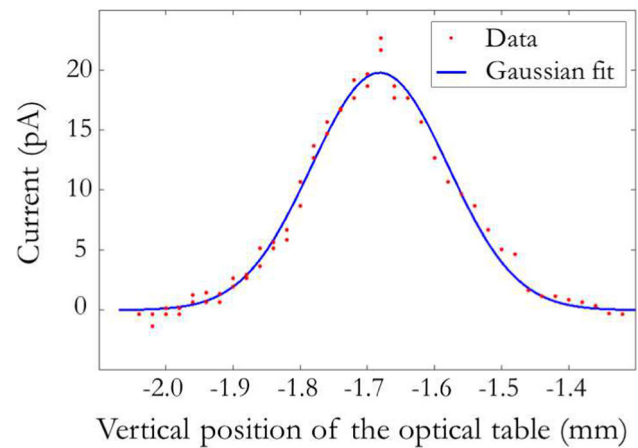
The first X-ray beam was produced during a scan of the optical cavity table to find the spatial position of the interaction point. These first photons were generated in a non-synchronized manner, i.e., without implementing temporal coincidences of electron bunches and the laser pulses. The laser power inside the Fabry–Perot cavity was 30 kW. X-rays were detected using the fluorescent screen detector located on the X-ray table in the bunker (cf. Fig. 5). This detector consists of a ZnCdS screen coupled to a photodiode. The signal is read with a picoammeter. This first X-rays signal is visible in Fig. 7. Also visible in the figure are the cross-checks realized to ensure that the signal is indeed due to X-rays (electron and laser beam shutters were closed or opened). Thanks to a calibration of the detector performed on the CRG-FAME/ESRF beamline [37] before its installation in ThomX and by taking into account the available angular aperture of our setup (half opening angle of 7 mrad), the total emitted flux can be deduced from the current measured by the photodiode and is: $F_{\text{tot}}^{\text{mes}} \sim 1.0 \times 10^7$ ph/s (full spectrum).

4.3 Measurements of transverse beam size and expected flux

Signals from the fluorescent screen detector were also recorded during a fine vertical scan of the optical table (micrometer steps). The data are shown in Fig. 8 (red points). Fitting this luminosity distribution with a Gaussian curve (see blue line in Fig. 8) leads to a root-mean-square $\sigma_{\text{lumi}} \sim 101$ μm . The waist of the laser pulses (Gaussian) was measured independently and is approximately equal to 130 μm (corresponding to $\sigma_L \sim 65$ μm). With this value of the laser pulse size, the luminosity distribution allows us first to deduce the transverse size of the electron bunch [5]: $\sigma_e = (\sigma_{\text{lumi}}^2 - \sigma_L^2)^{1/2} \sim 77$ μm and then to estimate the transverse size of

² Reference [31] indicates a transmission of 90%. Since then, correct adjustment of the focusing solenoid current value has enabled us to achieve a full transmission.

Fig. 8 Fluorescent screen detector signal (where the baseline has been subtracted) as a function of the vertical position of the Fabry–Perot optical table



the source from expression (3): $\sigma_S \sim 50 \mu\text{m}$. From these values of σ_e , σ_L , the average laser power stored in the cavity (30 kW), the average electron charge stored in the ring (estimated at between 30 pC and 80 pC during the data acquisition) and a factor taking into account the desynchronization of electrons bunches and laser pulses,³ the expected total flux calculated with expression (2) is: $F_{\text{tot}}^{\text{exp}} \sim 0.3 \times 10^7 - 3.3 \times 10^7 \text{ ph/s}$ which is in good agreement with the measured value by the fluorescence screen detector. The uncertainty in the expected value is due to the lack of knowledge of both the average electron charge stored in the ring and the desynchronization factor.

4.4 First X-ray spectrum

After receiving authorization from the ASN to open the safety shutter, X-rays were sent into the experimental hutch. Figure 9 shows the first measured X-ray spectrum, confirming that the signal in Fig. 7 is indeed a Compton X-ray signal. The spectrum was measured using a CdTe Amptek X-123 spectrometer positioned on the sample hexapod (cf. Fig. 6). The spectrometer's active surface is 25 mm^2 , the source-to-detector distance is $\sim 10.6 \text{ m}$, and the detector is positioned on-axis. Low energy peaks due to photons escaping after interactions with Cd or Te inside the detector are visible in the figure. An adjustment of the spectrum was performed with a Compton process model convolving purely kinematic effects with expressions characterizing the properties of the incident beams [8], the effects of the electron beam (energy spread and divergence) being largely dominant. Detector calibration was carried out with the data themselves, using the known K_α and K_β emission lines of Cd and Te [38]. The parameters resulting from the adjustment are an electron beam energy E_e of 49.3 MeV (in good agreement with the $\sim 50 \text{ MeV}$ expected and measured in the accelerator), an electron beam energy spread $\Delta E_e/E_e$ of 1.4 % and an electron beam divergence σ'_e of 3.3 mrad. The corresponding Compton edge E_m is 44.7 keV. The slight disagreement between the data spectrum and the fit at the right end of the spectrum is probably due to the fact that the energy distribution of the electron beam is not perfectly Gaussian.

4.5 First image of the beam

The first full-field image of the beam in the experimental area is shown in Fig. 10a. The image was recorded using a CdTe camera (Pilatus3 X CdTe 300K-W), with a size of $253 \text{ mm} \times 33 \text{ mm}$, a pixel size of $172 \mu\text{m}$ and a sensor thickness of 1 mm. The image was reconstructed by image stitching obtained by moving the detector vertically to scan the whole beam. The vacuum tube connecting the bunker and the experimental area is visible, as well as some mechanical supports for motorized detectors located on the first part of the line (inside the bunker) which were not retracted and remained in the beam path during image acquisition. The intensity profiles of the horizontal and vertical slices centered on the beam's maximum intensity (drawn by the dashed and dotted black lines) are shown in Fig. 10b and c, respectively.

To reconstruct the intensity distribution as a function of polar angle, camera pixels belonging to rings 2 mm wide of different radii, r_{det} , centered on the beam axis, were summed, and the corresponding polar angles with respect to the z -axis were calculated as follows: $\theta_{\text{det}} = r_{\text{det}}/D_{\text{det}}$, where D_{det} is the distance from the camera to the interaction point ($D_{\text{det}} \sim 10.6 \text{ m}$). The reconstructed intensity distribution, normalized to unity, is shown in Fig. 10d (red dots) for values of θ_{det} less than 2.5 mrad. The area corresponding

³ In unsynchronized X-ray production mode, the flux is divided by a factor 1000 to 2000; this factor is dependent on the repetition frequency (known), on the lengths of the laser pulses ($\sim 10 \text{ ps}$ measured) and on the length of the electron bunch at the interaction point, expected to be around 10 ps, but not yet measured.

Fig. 9 First ThomX X-ray spectrum acquired with a CdTe Amptek X-123 spectrometer and result of the fit. The small peaks around 17 keV are due to secondary X-rays produced by interaction with Cd or Te and escaping from the detector

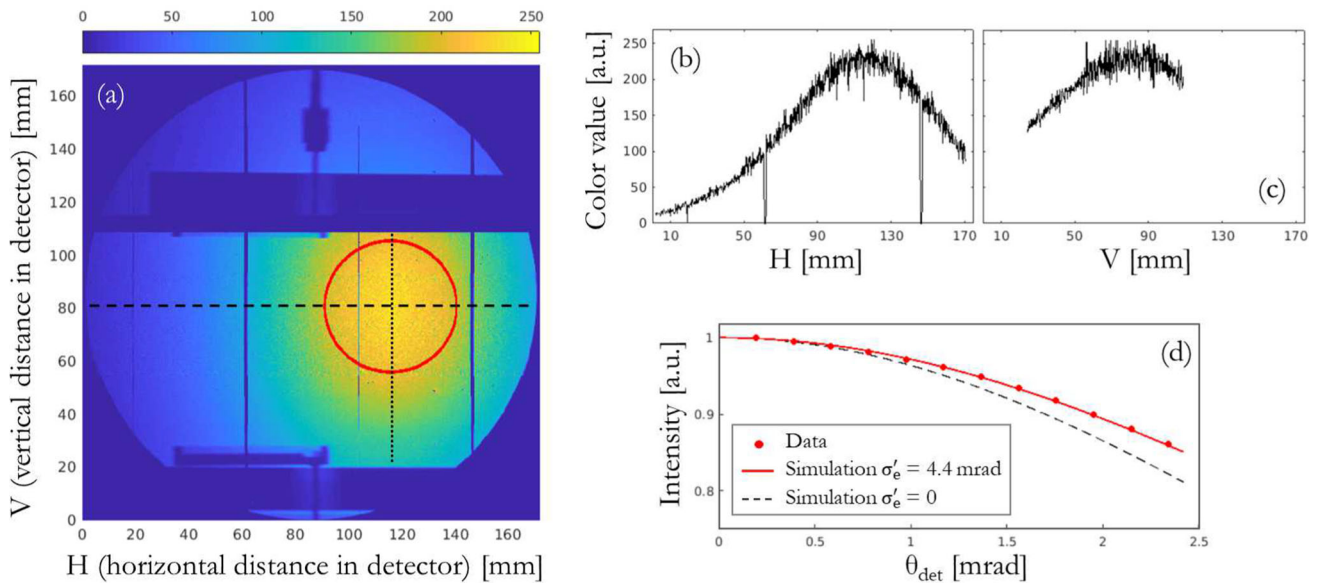
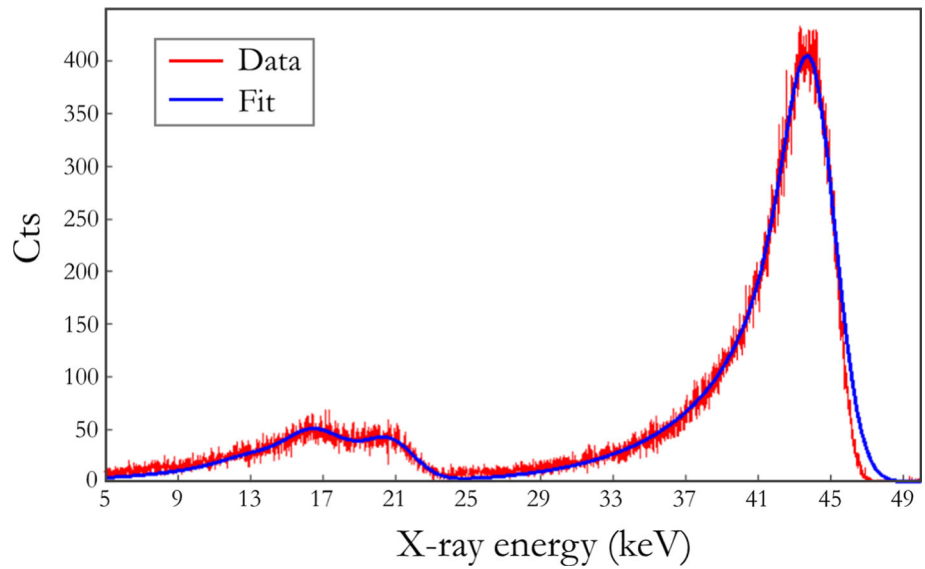


Fig. 10 First full-field image of the X-ray beam acquired with a Pilatus CdTe camera **a**. Intensity profiles along dashed **b** and dotted **c** black lines drawn on the image. Intensity distribution (normalized to the unity) as a function of the polar angle θ_{det} **d** for camera data (red points), simulation with $\sigma'_e = 4.4$ mrad (red full line), simulation with $\sigma'_e = 0$ (dashed black line). The region delimited by the red circle on the image delimits the area $\theta_{det} < 2.5$ mrad

to $\theta_{det} < 2.5$ mrad is delimited by the red circle in Fig. 10a. The dependence of the intensity on the scattering angle θ_X (defined in Fig. 1) is written as follows [8]:

$$I(\theta_X) \sim \frac{1 + (\gamma^2 \theta_X^2)^2}{(1 + \gamma^2 \theta_X^2)^4}. \tag{6}$$

For an electron moving along the z -axis, θ_X^2 in formula (6) is equal to θ_{det}^2 . For an electron making a polar angle θ_e with the z direction, θ_X^2 is written as [8]: $\theta_X^2 \sim \theta_{det}^2 + \theta_e^2$, as long as θ_{det} and θ_e are small (i.e., $\sin \theta_e \sim \theta_e$ and $\sin \theta_{det} \sim \theta_{det}$). The experimental intensity distribution has been adjusted with expression (6) convolved with the probability distribution of θ_e^2 : $dp/d\theta_e^2 = 1/(2\sigma_e'^2) \exp[-\theta_e^2/(2\sigma_e'^2)]$ [8]. An electron beam divergence σ_e' equal to ~ 4.4 mrad leads to the best adjustment (shown in solid red line in Fig. 10d) and is quite similar to the value of 3.3 mrad deduced from the X-ray spectrum (c.f. Subsect. 4.5). To visualize the order of magnitude of the influence of the electron beam divergence on the distribution, the simulated distribution for $\sigma_e' = 0$ is also shown in Fig. 10d (dashed black line).

Table 1 Current and future electron, laser and X-ray beams parameters

	Today	Near future	Next future	Unit
Electron/laser synchronization	No	Yes	Yes	
Electron energy	50	50–70	50–70	MeV
Avg stored electron charge	0.05	0.5	1	nC
Avg stored laser power	30	100	700	kW
Electron spot size at IP (rms)	77	77	77	(μm)
Laser spot size at IP (rms)	65	65	40	(μm)
X-ray Compton edge	45	45–90	45–90	keV
Avg total flux	2.10^7	6.10^{11}	1.10^{13}	ph/s

5 Conclusion and outlook

We produced the first X-ray beam with ThomX and acquired the first spectrum and image of the beam in the experimental area. A flux of $\sim 10^7$ ph/s (full spectrum) was produced in a mode of unsynchronized electron/laser collisions. A fit of the spectrum enabled us to deduce the energy, energy spread and divergence values of the electron bunches, and then obtain the energy value of the on-axis Compton photons (44.7 keV). The divergence of the electron beam can also be deduced from the intensity distribution with respect to the polar scattering angle and was found to be quite similar to the value obtained from the spectrum.

In the near future, we will implement synchronized coincidences of the electron bunches and laser pulses (a gain of 1000 to 2000 is expected for the flux). We will also increase the electron bunch charge stored in the ring by a factor of ~ 10 by increasing the charge delivered by the injector⁴ on the one hand, and improving the matching between the transfer line and the ring on the other. Electron energy will be boosted to reach 70 MeV⁴. We will also increase the power stored in the optical cavity to ~ 100 kW by increasing the power injected into the cavity and improving the coupling of laser pulses into the cavity. With these improvements, the total flux will reach $F_{\text{tot}} \sim 5 \times 10^{11}$ ph/s. In the slightly more distant future, an electron charge of 1 nC and laser power of 700 kW stored in the ring and Fabry–Perot cavity, respectively, as well as a decrease in the transverse size of laser pulses to 40 μm are planned and will allow producing $\sim 10^{13}$ X-rays/s in the 45–90 keV energy range. Table 1 summarizes the ThomX parameters expected in the near future, those achievable in the more distant future, and indicates the corresponding X-ray energies and fluxes.

Once we will have achieved a stable flux of $\sim 10^{11}$ X-rays/s, the main analysis techniques used in X-ray research will be qualified in the experimental hutch. We will demonstrate the source's potential and limitations in the field of imaging (standard imaging, propagation-based phase contrast imaging, K-edge subtraction imaging and tomography). Using phantoms of low-density materials with properties comparable to those of soft tissue, we will measure spatial resolution and contrast, assess sensitivity to contrast drugs, determine the minimum exposure time required, and demonstrate the absence of beam-hardening effects thanks to the beam's quasi-monochromaticity. In addition, after commissioning and characterizing our monochromator and focusing device, we will set up simple demonstration experiments by illuminating crystal or powder samples to qualify our source in terms of sensitivity and resolution in fluorescence spectroscopy and diffraction analysis techniques. For this, a pink beam or a monochromatic beam, the naturally divergent beam or a focused beam will be used. Finally, we will be studying the feasibility of the XANES (X-ray Absorption Near Edge Structure) and EXAFS (Extended X-Ray Absorption Fine Structure) techniques [39, 40] with the ThomX beam.

Several experiments or proofs of principle of some analysis techniques currently achievable only in synchrotrons have been carried out at the MuCLS source and have shown promising results [41]. The advantages and the interests of a high-intensity compact Compton source installed in an university, a museum or an hospital are obvious. The current advances in this area pave the way for the transfer of synchrotron techniques into lab-scale environments. The brightness that ThomX will be capable to achieve will be decisive as to the feasibility, quality and efficiency of each of the above-mentioned analysis techniques.

Acknowledgements The present work is financed by the French National Research Agency (ANR) under the Equipex program ANR-EQPX-51.

Data Availability Statement Data supporting the results reported in this paper were generated at ThomX and are available from the corresponding author on request. The manuscript has associated data in a data repository.

References

1. Z. Huang, R.D. Ruth, Laser-electron storage ring. *Phys. Rev. Lett.* **80**(5), 979–979 (1998). <https://doi.org/10.1142/S1793626810000440>
2. G.A. Krafft, G. Priebe, Compton sources of electromagnetic radiation. *Rev. Accel. Sci. Technol.* **3**, 147–163 (2010). <https://doi.org/10.1142/S1793626810000440>
3. P. Walter et al., A new high quality x-ray source for cultural heritage. *C. R. Phys.* **10**(7), 676–690 (2009). <https://doi.org/10.1016/j.crhy.2009.09.001>

⁴ To do this, we must first obtain an authorization from the ASN.

4. M. Jacquet, High intensity compact Compton X-ray sources: challenges and potential of applications. Nucl. Instr. Meth. Phys. Res. B **331**, 1–5 (2014). <https://doi.org/10.1016/j.nimb.2013.10.078>
5. T. Suzuki, *General Formulas of Luminosity for Various Types of Colliding Beam Machines KEK-76-3* (National Laboratory for High Energy Physics, Oho, Ibaraki (Japan), 1976)
6. W.J. Brown, F.V. Hartemann, Brightness optimization of ultra-fast Thomson scattering X-ray sources. AIP Conf. Proc. **737**, 839–845 (2004). <https://doi.org/10.1063/1.1842631>
7. K.E. Deitrick et al., High-brilliance, high-flux compact inverse Compton light source. Phys. Rev. Accel. Beams **21**, 080703 (2018). <https://doi.org/10.1103/PhysRevAccelBeams.21.080703>
8. M. Jacquet, C. Bruni, Analytic expressions for the angular and the spectral fluxes at Compton X-ray sources. J. Synchrotron Radiat. **24**, 312–322 (2017). <https://doi.org/10.1107/S1600577516017227>
9. A. Arnold, J. Teichert, Overview on superconducting photoinjectors. Phys. Rev. ST Accel. Beams **14**, 024801 (2011). <https://doi.org/10.1103/PhysRevSTAB.14.024801>
10. R. Xiang, A. Arnold, J.W. Lewellen, Superconducting radio frequency photoinjectors for CW-XFEL. Front. Phys. **23**, 1166179 (2023). <https://doi.org/10.3389/fphy.2023.1166179>
11. M. Jacquet, P. Suortti, Radiation therapy at compact Compton sources. Phys. Med. **31**, 596–600 (2015). <https://doi.org/10.1016/j.ejmp.2015.02.010>
12. M. Jacquet, Potential of compact Compton sources in the medical field. Phys. Med. **32**, 1790–1794 (2016). <https://doi.org/10.1016/j.ejmp.2016.11.003>
13. E. Eggl et al., The Munich compact light source: initial performance measures. J. Synchrotron Radiat. **23**, 1137–1142 (2016). <https://doi.org/10.1107/S160057751600967X>
14. B. Günther et al., The Munich compact light source: flux doubling and source position stabilization at a compact Inverse-Compton synchrotron X-ray source. Microsc. Microanal. **24**(S2), 312–313 (2018). <https://doi.org/10.1017/S1431927618013892>
15. P. Yu, W. Huang, Lattice design and beam dynamics in a compact X-ray source based on Compton scattering. Nucl. Instr. Meth. A **592**, 1–8 (2008)
16. T. Rui, W. Huang, Lattice design and beam dynamics of a storage ring for a Thomson scattering x-ray source. Phys. Rev. Accel. Beams **21**, 100101 (2018). <https://doi.org/10.1103/PhysRevAccelBeams.21.100101>
17. E.G. Bessonov et al., Design study of compact laser-electron X-ray generator for material and life sciences applications. JINST **4**, P07017 (2009)
18. E. Bulyak et al., Compact X-ray source based on Compton backscattering. Nucl. Instr. Meth. A **487**, 241–248 (2002)
19. A. Variola, The ThomX project. Proceedings of 2nd International Particle Accelerator Conference WEOAA01, 1903–1905 (2011). <https://hal.in2p3.fr/in2p3-00635646>
20. J. Urakawa, Development of a compact X-ray source based on Compton scattering using a 1.3 GHz superconducting RF accelerating Linac and a new laser storage cavity. Nucl. Instrum. Meth. A **637**, S47–S50 (2011)
21. J. Urakawa, *Overview for Quantum Beam Project at KEK* (Tomsk Polytechnic University, Tomsk, 2012)
22. R. Hajima et al., Detection of radioactive isotopes by using laser Compton scattered γ -ray beams. Nucl. Instrum. Meth. A **608**, S57–S61 (2009)
23. W.S. Graves et al., MIT inverse Compton source concept. Nucl. Instr. Meth. Phys. Res. A **608**, S103–S105 (2009)
24. R. Ainsworth et al., Asymmetric dual axis energy recovery Linac for ultrahigh flux sources of coherent x-ray and THz radiation: investigations towards its ultimate performance. Phys. Rev. Accel. Beams **19**, 083502 (2016). <https://doi.org/10.1103/PhysRevAccelBeams.19.083502>
25. P. Cardarelli et al., BriXS, a new X-ray inverse Compton source for medical applications. Phys. Med. **77**, 127–S137 (2020). <https://doi.org/10.1016/j.ejmp.2020.08.013>
26. K.E. Deitrick et al., High-brilliance, high-flux compact inverse Compton light source. Phys. Rev. Accel. Beams **21**, 080703 (2018). <https://doi.org/10.1103/PhysRevAccelBeams.21.080703>
27. W.S. Graves et al., Compact x-ray source based on burst-mode inverse Compton scattering at 100 kHz. Phys. Rev. ST Accel. Beams **17**, 120701 (2014). <https://doi.org/10.1103/PhysRevSTAB.17.120701>
28. A. Snigirev et al., A compound refractive lens for focusing high-energy X-rays. Nature **384**, 49–51 (1996)
29. A. Variola et al., *ThomX Technical Design Report* (LAL, Orsay, 2014), p.164
30. K. Dupraz et al., The ThomX ICS source. Phys. Open **5**, 100051 (2020). <https://doi.org/10.1016/j.physo.2020.100051>
31. C. Bruni et al., First electron beam of the ThomX project. Proceedings of the 13th International Particle Accelerator Conference, Bangkok, Thailand, (JACoW), p. 1632–1635 (2022). <https://doi.org/10.18429/JACoW-IPAC2022-WEOYSP2>
32. V. Kubytskyi et al., Commissioning of the ThomX storage ring. Proceedings of the 14th International Particle Accelerator Conference, Venice, Italy, (JACoW), p. 1141–1143 (2023). <https://doi.org/10.18429/JACoW-IPAC2023-MOPM069>
33. A. Moutardier et al., Characterisation of the electron beam visualization stations of the ThomX accelerator. Proceedings of the 13th International Particle Accelerator Conference, Bangkok, Thailand, (JACoW), p. 240–243 (2022). <https://doi.org/10.18429/JACoW-IPAC2022-MOPOPT006>
34. N. Delerue et al., The synchronisation system of the ThomX accelerator. Proceedings of the 9th International Particle Accelerator Conference, Vancouver, BC, Canada, (JACoW), p. 2243–2246 (2018). <https://doi.org/10.18429/JACoW-IPAC2018-WEPAL035>
35. L. Amoudry, *Etude de Cavités Fabry–Perot de Hautes Finesses Pour le Stockage de Fortes Puissances Moyennes. Application à la Source Compacte de Rayons X ThomX* (Université Paris-Saclay, Paris, 2021)
36. L. Amoudry et al., Modal instabilities suppression in high average power and high finesse Fabry–Perot cavity. Appl. Opt. **59**(1), 116–121 (2019). <https://doi.org/10.1364/AO.59.000116>
37. O. Proux et al., FAME: a new beamline for x-ray absorption investigations of very-diluted systems of environmental, material and biological interests. Phys. Scr. **115**, 970–973 (2005). <https://doi.org/10.1238/Physica.Topical.115a00970>
38. R.H. Redus et al., Characterization of CdTe detectors for quantitative X-ray spectroscopy. IEEE Trans. Nuclear Sci. **56**(4), 2524–2532 (2009). <https://doi.org/10.1109/TNS.2009.2024149>
39. A. Bianconi, Surface X-ray absorption spectroscopy: surface EXAFS and surface XANES. Appl. Surf. Sci. **6**, 392–418 (1980)
40. J.B. Pendry et al., Multiple-scattering resonances and structural effects in the x-ray-absorption near-edge spectra of Fe II and Fe III hexacyanide complexes. Phys. Rev. B **26**(12), 6502–6508 (1980)
41. B. Günther et al., The versatile X-ray beamline of the Munich compact light source: design, instrumentation and applications. J. Synchrotron Radiat. **27**, 1395–1414 (2020). <https://doi.org/10.1107/S1600577520008309>

Springer Nature or its licensor (e.g. a society or other partner) holds exclusive rights to this article under a publishing agreement with the author(s) or other rightsholder(s); author self-archiving of the accepted manuscript version of this article is solely governed by the terms of such publishing agreement and applicable law.